Impacts of sub-grid topographic representations on surface energy balance and boundary conditions in the E3SM Land Model

Dalei Hao[1], Gautam Bisht[1], Meng Huang[1], Po-Lun Ma[1], Teklu Tesfa[1], Wei-Liang Lee[2], Yu Gu[3], L. Ruby Leung[1]

[1]Atmospheric Sciences and Global Change Division, Pacific Northwest National Laboratory, Richland, WA, USA

[2]Research Center for Environmental Changes, Academia Sinica, Taipei, Taiwan

[3]Joint Institute for Regional Earth System Science and Engineering and Department of Atmospheric and Oceanic Sciences, University of California, Los Angeles, CA, USA

Corresponding author: Dalei Hao (`dalei.hao@pnnl.gov`)

Key Points:

- ELM was used to evaluate the impacts of sub-grid topographic representations
- Subgrid topographic representation has large impacts on surface energy balance and surface boundary conditions
- Topounit provides better performance than the default sub-grid structure in ELM

Abstract

Sub-grid topographic heterogeneity has large impacts on surface energy balance and land-atmosphere interactions. However, the impacts of representing sub-grid topographic effects in land surface models (LSMs) on surface energy balance and boundary conditions remain unclear. This study analyzed and evaluated the impacts of sub-grid topographic representations on surface energy balance, turbulent heat flux and scalar (co-)variances in the Energy Exascale Earth System Model (E3SM) land model (ELM). Three sub-grid topographic representations in ELM were compared: (1) the default sub-grid structure (D), (2) the recently developed sub-grid topographic structure (T), and (3) high spatial resolution (1KM). Additionally, two different solar radiation schemes in ELM were compared: (1) the default plane-parallel radiative transfer scheme (PP) and (2) the parameterization scheme (TOP) that accounts for sub-grid topographic effects on solar radiation. A series of simulations with the three grid structures (D, T and 1KM) and two treatments of solar radiation (TOP and PP) were carried out in the Sierra Nevada, California. There are significant differences between TOP and PP in the 1-km simulated surface energy balance, but the differences in the mean values and standard deviations become small when aggregated to the grid-scale (i.e., 0.5°). The T configuration better mimics the 1KM simulations than the D configuration, and better captures the sub-grid topographic effects on surface energy balance as well as surface boundary conditions. These results underline the importance of representing sub-grid topographic heterogeneities

in LSMs and motivate future research to understand the sub-grid topographic effects on land-atmosphere interactions over mountain areas.

Plain Language Summary

Topography has significant impacts on surface energy balance and land-atmosphere interactions, which has not been well represented in land surface models (LSMs). Our study quantified the impacts of representing sub-grid topography on surface energy balance and surface boundary conditions in the Energy Exascale Earth System Model (E3SM) land model (ELM). The topounit-based sub-grid structure that parsimoniously captures sub-grid topographic heterogeneity provides a better performance than the default sub-grid structure in ELM and is computationally efficient. Our study underlines the importance of representing sub-grid topographic heterogeneities in LSMs and earth system models (ESMs) and is promising to promote future research to understand the sub-grid topographic effects on terrestrial processes and land-atmosphere interactions over complex terrain.

1 Introduction

Ubiquitous heterogeneity of the land surface plays a pivotal role in surface energy balance and land-atmosphere exchanges of momentum, heat and water (Bou-Zeid et al., 2020; de Vrese et al., 2016; Levy et al., 2020). Sub-grid heterogeneity comprises of spatial variabilities in land use/land cover (LULC) types, soil characteristics, and topography (Giorgi and Avissar, 1997). Sub-grid heterogeneity affects the surface energy partitioning, modifies the vertical structure of the planetary boundary layer (PBL), creates mesoscale atmospheric circulations, and affects cloud formation and regional climate (Brunsell et al., 2011; Chen et al., 2020; Lee et al., 2019a; Maronga and Raasch, 2013; Wu et al., 2009; Zhang et al., 2010; Zheng et al., 2021). Accounting for sub-grid heterogeneities of land surface plays a vital role in land surface modeling and land-atmosphere coupling (de Vrese et al., 2016; Fisher and Koven, 2020).

Topographic variability, an important heterogeneous feature of the land surface, has large impacts on many land surface processes. Topography fundamentally organizes water, energy, and biogeochemical processes at hillslope scales by modifying the downwelling solar radiation at the land surface and laterally transporting water from ridges to valleys (Fan et al., 2019). By geometric shadowing, topography causes a strong contrast of incoming solar radiation between sunny and shady slopes (Hao et al., 2019; Proy et al., 1989). While valleys generally receive less diffuse radiation than hilltops due to the obstructions from adjacent slopes, they receive more multi-scattering radiation from adjacent slopes (Dubayah, 1992). The variability in the incoming solar radiation leads to spatial variability in soil and vegetation characteristics that follow the topographic distributions (Ropars and Boudreau, 2012). For instance, north-facing and south-facing slopes support different vegetation types and species diversities (Dearborn and Danby, 2017). Representing these topo-

graphic effects on incoming solar radiation as well as the topography-dependent soil and vegetation distributions at sub-grid levels in coarse resolution global land surface models (LSMs) is necessary for accurately resolving terrestrial processes in regions with heterogeneous terrain.

While sub-grid heterogeneity of LULC is routinely accounted for in LSMs, the sub-grid variability due to topography has often been neglected. LSMs account for LULC heterogeneity using a computationally efficient tiling approach in which a coarse-scale grid cell is statistically or geographically divided into sub-grid cells, each of which is a single LULC type. For example, the Community Land Model Version 5.0 (CLM5.0) (Lawrence et al., 2019) and the Energy Exascale Earth System Model (E3SM) land model Version 1 (ELMv1) (Golaz et al., 2019) use a nested sub-grid hierarchical structure where each grid is statistically composed of multiple land units, each land unit can have multiple soil columns, and each soil column can have multiple Plant Functional Types (PFTs). These existing sub-grid schemes neglect the joint distributions of sub-grid topography, soil and vegetation. Sub-grid heterogeneities can also be represented by running LSMs at high spatial resolutions (~1 km), but this method is computationally prohibitive for global Earth System Models. Recently, high-resolution Digital Elevation Model (DEM) data has been used to add topography-based sub-grid structures in LSMs, including CLM and ELM (Chaney et al., 2016; Fiddes and Gruber, 2012; Ke et al., 2013; Tesfa and Leung, 2017). Tesfa and Leung (2017) extended the default sub-grid scheme of ELM by introducing topographic units (topounits), each associated with different topographic features. In the new sub-grid scheme, a ELM coarse-scale grid (0.5° or coarser) can have multiple topounits and each topounit can have multiple landunits, soil columns and PFTs. In addition, most existing LSMs adopt a two-stream solar radiative transfer scheme with the plane-parallel (PP) assumption that neglects the sub-grid topographic effects on solar radiation (Sellers, 1985). Recently, a scheme (TOP) to account for the sub-grid topographic effects on solar radiation has been implemented in ELM (Hao et al., 2021). The aforementioned improvements in ELM offer a great opportunity to study the sub-grid topographic effects on land surface processes.

How sub-grid topographic representations in LSMs may affect the simulated surface energy balance and surface boundary conditions is unclear. Sub-grid topography can affect the radiative transfer processes and hence, influence the surface energy balance (Hao et al., 2021). The mean surface turbulent heat flux (e.g., latent heat and sensible heat fluxes) (Lyons and Halldin, 2004) and high-order scalar (co-)variances (i.e., the variances and covariances of scalar quantities such as near-surface temperature and humidity) are used in atmospheric turbulence parameterization of ESMs for land-atmosphere coupling (Guo et al., 2015). These surface boundary conditions are crucial for simulating atmospheric flows and circulations in Earth system models (Machulskaya and Mironov, 2018). Different representations of sub-grid heterogeneity in LSMs can lead to different surface turbulent heat flux and scalar (co-)variances that can in turn affect the associated PBL processes (Román-Cascón

et al., 2021). ELM can be configured in three different ways to capture the sub-grid heterogeneity: (i) a coarse-resolution simulation (denoted as D) with the default sub-grid structure that excludes sub-grid topographic heterogeneity, (ii) a coarse-resolution simulation (denoted as T) with topounit-based sub-grid structure that parsimoniously captures sub-grid topographic heterogeneity, and (iii) a high-resolution (i.e., 1 km) simulation (denoted as 1KM) that explicitly accounts for sub-grid heterogeneity. Generally the 1KM simulations with spatially-explicit sub-grid heterogeneity can be regarded as a reference simulation (Schneider et al., 2017). The accuracy of the D- and T-based simulations to simulate the surface energy budget and surface boundary conditions over heterogeneous terrain needs to be evaluated. In addition, the role of sub-grid topography within solar radiative transfer schemes (i.e., TOP and plane parallel (PP)) on surface energy balance terms and surface boundary conditions deserves further investigations.

The objective of this study is to analyze the effects of sub-grid topographic heterogeneity on surface energy balance and surface boundary conditions for turbulent heat flux and scalar (co-)variances. Land surface parameters at 1 km spatial resolution were first developed based on existing high-resolution datasets for vegetation, soil and DEM. Then a series of ELM simulations with three different sub-grid topographic representations (D, T and 1KM) and two solar radiation radiative transfer schemes (TOP and PP) were carried out over a region of heterogeneous terrain. The surface boundary conditions for the variance and co-variance quantities under different cases were next derived using the method of (Machulskaya and Mironov, 2018), which is suitable for analyzing results over heterogeneous surfaces. Finally, the effects of sub-grid topographic representations in ELM on surface energy balance and boundary conditions were analyzed and discussed.

2 Materials and Methods

2.1 Study area

A representative 1° grid (38°N -39°N, 120.5°W-119.5°W) in the Sierra Nevada, California with heterogeneous distribution of topography was selected as a testbed in the study. The study area covers various topographic features such as hill, ridge, valley and saddle with elevation ranging from 330 m to 3418 m (Figure 1a) and slope (Figure 1b) varying from 0° (i.e., flat surface) to 41° (i.e., steep slope). The study region is mainly dominated by forests (southwest) and shrubland/grasslands (northeast), with a few small urban areas, croplands and lakes (Figure 1c). The southwestern regions have higher leaf area index (LAI), organic matter density, clay and silt contents and lower sand contents than the northeastern regions (Figure 1d-h).

2.2 High-resolution land surface datasets for ELM

In this study, a series of high-resolution, sub-kilometer datasets for vegetation, soil and topography were collected to develop spatially-continuous land surface parameters at 1 km for ELM (Table 1) following the methods in Ke et al. (2012).

MODIS 500 m land cover and LAI data were acquired from the Google Earth Engine (GEE) (Gorelick et al., 2017). Specifically, the IGBP land cover classification data in the yearly 500 m MCD12Q1 V6 land cover type product (Friedl et al., 2002) for the year 2010 was used to determine lake, wetland, urban and PFTs based on the methods in (Bonan et al., 2002; Ke et al., 2012). The IGBP classification scheme was first converted to ELM's PFTs that are composed of needleleaf evergreen trees, needleleaf deciduous trees, broadleaf evergreen trees, broadleaf deciduous trees, shrub, grass and crop. The WorldClim V1 30 arc-seconds monthly climatological temperature and precipitation data (Hijmans et al., 2005) were further used to classify the PFTs into tropical, temperate and boreal climate groups based on the rules presented by (Bonan et al., 2002). The fractions of C3 and C4 grasses were derived using the method in Still et al. (2003). The monthly LAI time series were derived based on the 4-day 500 m MCD15A3H V6 LAI product (Myneni et al., 2002) from 2003-2010. The methodology in Zeng et al. (2002) was used to calculate monthly stem area index (SAI) from the monthly LAI data.

The Soilgrid v2 data with 250 m resolution (Poggio et al., 2021) was used to represent high-resolution soil characteristics. This data was generated using site-level soil profile data and remote sensing-based soil covariates and machine learning methods trained based on site-level soil profile data (Hengl et al., 2017). Specifically, organic matter density, percent clay and percent sand at seven standard depths (i.e., 0, 5, 15, 30, 60, 100 and 200 cm) were used to derive corresponding soil organic matter and structure in ELM.

The Shuttle Radar Topography Mission (SRTM) DEM data (Rabus et al., 2003) with 90 m spatial resolution was used to derive topography-related parameters including mean elevation, mean slope, standard deviation of elevation. This data was also used to derive 1 km topographic factors used in the parameterization of sub-grid topographic effects on solar radiation in ELM (see Section 2.3).

The default values were used for all other land surface parameters in ELM. The soil and topography datasets were re-sampled to 1 km spatial resolution using area-weighted average methods, while the vegetation dataset was aggregated to 1 km using majority resampling methods.

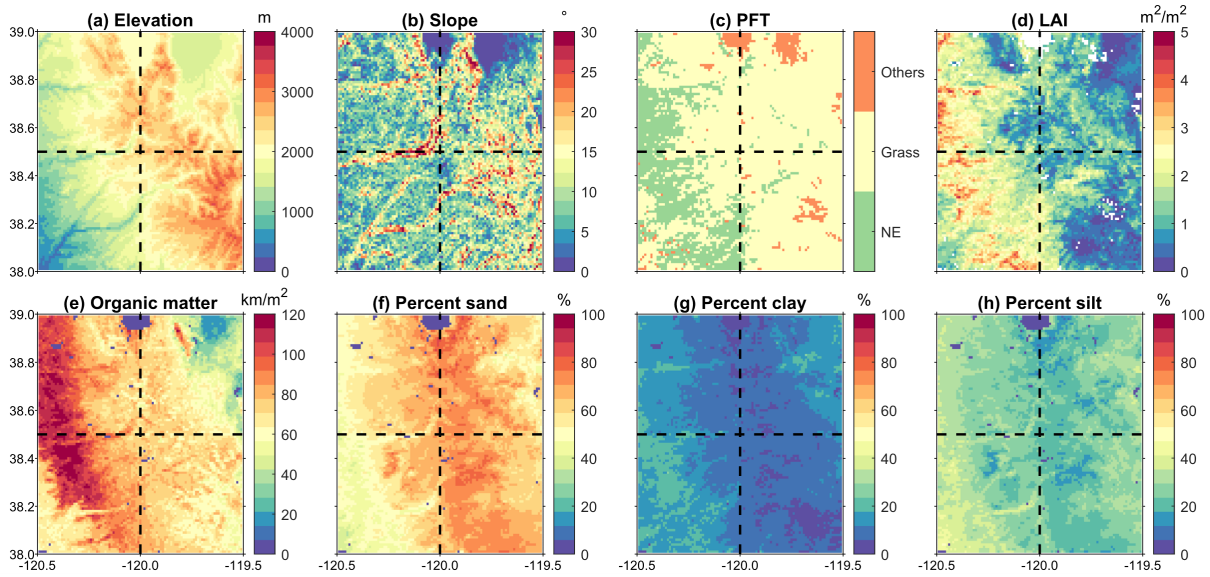

Figure 1. Spatial distributions of (a) elevation, (b) slope, (c) PFT, (d) LAI in August, (e) organic matter density and (f-h) percentages of sand, clay and silt (d-e), respectively over the study area at 1 km resolution. In (c), NE, Grass and Others represent the Needleleaf Evergreen Trees-Temperate, C3 grass and other PFTs in ELM.

1. **Table 1. Specifications of high-resolution datasets used in this study.**

@ >p(- 12) * >p(- 12) * >p(- 12) * >p(- 12) * >p(- 12) * >p(- 12) * >p(- 12) * @ Group & Parameter & Data source & Period & Spatial resolution (m) & Temporal resolution & References
Climate & Temperature & WorldClim V1 & Climatological & 1000 & monthly & (Hijmans et al., 2005)
& Precipitation & WorldClim V1 & Climatological & 1000 & monthly & (Hijmans et al., 2005)
Vegetation & Land cover & MODIS & 2010 & 500 & yearly & (Friedl et al., 2002)
& Leaf area index & MODIS & 2003-2010 & 500 & 4-day & (Myneni et al., 2002)
& Stem area index & Derived from LAI & 2003-2010 & 500 & 4-day & (Myneni et al., 2002)
Soil & Organic matter density & Soilgrid v2 & [-] & 250 & [-]

[-]

[-] & (Poggio et al., 2021)
& Percent sand & Soilgrid v2 & [-] & 250 & & (Poggio et al., 2021)
& Percent clay & Soilgrid v2 & [-] & 250 & & (Poggio et al., 2021)

Topography & Elevation & SRTM DEM & [-] & 90 & [-] & (Rabus et al., 2003)

2.3 Sub-grid topographic improvements in ELM

E3SM, supported by the U.S. Department of Energy (DOE), is an advanced Earth system model developed to address the grand challenge of actionable predictions of Earth system variability and change (Leung et al., 2020). ELM version 1 (ELMv1) originated from CLM4.5 and has incorporated a few new features, such as a new variably saturated flow model (Bisht et al., 2018) and an updated module for phosphorus cycle dynamics (Yang et al., 2019).

Recently, a new sub-grid topographic structure (topounit) has been included in ELM to improve the representation of sub-grid topographic effects on land surface processes (Tesfa and Leung, 2017). Specifically, each 0.5° grid is divided into different topounits based on the topographic attributes composed of elevation, slope and aspect. The study area includes four different 0.5° grids (i.e., G1, G2, G3 and G4) and each grid includes 11 topounits (Figure 2). These four grids show different topographic features and topounit distributions. The spatial patterns of topounits in Figure 2 generally follow the spatial distribution of elevation in Figure 1a. Different topounits have different elevation ranges. For instance, the elevation of topounit-1 for G1 ranges from 1040 m to 1713 m, and that of topounit-11 ranges from 2303 m to 2952 m. Besides, each topounit can have its own PFT and soil characteristics.

In addition, a parameterization of sub-grid topographic effects on solar radiation has been implemented in ELM (Hao et al., 2021). This cost-effective parameterization uses multiple linear regression methods to build the relationship between several topographic factors and sub-grid topographic effects (Lee et al., 2011). The topographic factors include the standard deviation of elevation, grid-average cosine of the local solar incident angle, sky view factor and terrain configuration factor, which are pre-computed based on the 90 m SRTM data (Table 1). This parameterization has been successfully applied in the Weather Research and Forecasting (WRF), CLM4 and ELM at different spatial scales ranging from 800 m to 200 km (Hao et al., 2021; Lee et al., 2019b; Zhao et al., 2016).

In this study, we used ELMv1 with the two abovementioned sub-grid topographic improvements to analyze the effects of sub-grid topographic representations on surface energy balance and boundary conditions.

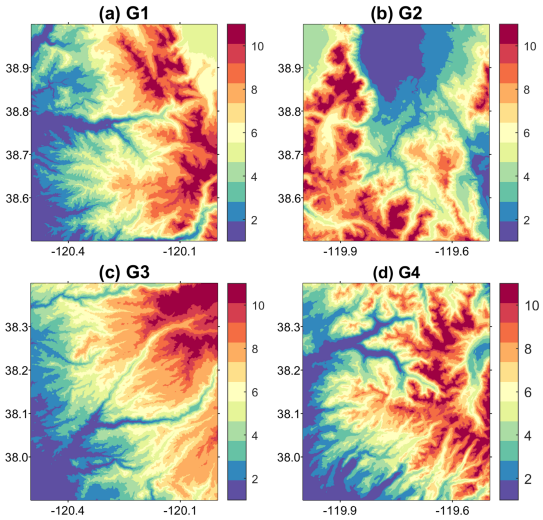

Figure 2. Spatial patterns of topounits within four different 0.5° × 0.5° grids.

2.4 Computation of surface boundary conditions of scalar (co-)variances

Most of the existing Earth system models couple the land and atmosphere using grid-scale mean fluxes and state variables, thus ignoring the effects of sub-grid heterogeneity. For instance, the current version of E3SM couples the land and atmosphere at the grid-level (André et al., 1978), which assumes land-atmosphere interaction are dominated by spatially homogeneous processes, so this method is hereafter referred to as the HOM method. In contrast, Machulskaya and Mironov (2018) developed a patch(tile)-based method that accounts for the effects of sub-grid heterogeneity. Hereafter, this method is referred to the HET method. Specifically, when considering the heterogeneity of the underlying surface as composed of different patches, a generic variable x can be decomposed into three components (Avissar and Chen, 1993):

$$x = \langle \overline{x}_p \rangle + \overline{x}_p{}'' + x_{\mathrm{sp}} \quad (1)$$

where $\langle \overline{x}_p \rangle$ represents the average value over a grid, $\overline{x}_p$ represents the average value over the p$^{\mathrm{th}}$ patch, $\overline{x}_p{}''$ $(= \overline{x}_p - \langle \overline{x}_p \rangle)$ represents an average fluctuation of a patch-level value away from the grid-level average value, and x_{sp} represents a sub-patch-level fluctuation. Here we define the sum of the patch- and grid-level fluctuations as

$$x' = \overline{x}_p{}'' + x_{\mathrm{sp}} \quad (2)$$

By construction, $\langle \overline{x}_p{}'' \rangle$=0 and $\overline{x_{\mathrm{sp}}}$=0, i.e., the grid-level average value of the patch-level fluctuations and the patch-level average value of the sub-patch level

fluctuations are zero (Machulskaya and Mironov, 2018). Then the scalar variance for any quantity x (e.g., temperature and humidity) denoted by $\left\langle x^{'2} \right\rangle$, can be derived as the sum of sub-patch- and patch-level variances:

$$\left\langle x^{'2} \right\rangle = \left\langle \overline{(\overline{x}_p^{''} + x_{\mathrm{sp}}) \bullet (\overline{x}_p^{''} + x_{\mathrm{sp}})} \right\rangle = \left\langle \overline{x}_p^{''2} \right\rangle + \left\langle \overline{x_{\mathrm{sp}}^2} \right\rangle \quad (3)$$

Similarly, the scalar co-variance between two quantities, x and y, (e.g. temperature and humidity), can be calculated as

$$\left\langle x^{'} y^{'} \right\rangle = \left\langle \overline{(\overline{x}_p^{''} + x_{\mathrm{sp}}) \bullet (\overline{y}_p^{''} + y_{\mathrm{sp}})} \right\rangle = \left\langle \overline{x}_p^{''} \overline{y}_p^{''} \right\rangle + \left\langle \overline{x_{\mathrm{sp}} y_{\mathrm{sp}}} \right\rangle \quad (4)$$

The discrete forms of Eqs. (3-4) can be expressed as

$$\left\langle x^{'2} \right\rangle = \sum_1^n f_p \bullet \left(\overline{x}_p - \left\langle \overline{x}_p \right\rangle\right)^2 + \sum_1^n f_p \bullet \overline{x_{\mathrm{sp}}^2} \quad (5)$$

$$\left\langle x' y' \right\rangle = \sum_1^n f_p \bullet \left(\overline{x}_p - \left\langle \overline{x}_p \right\rangle\right) \bullet \left(\overline{y}_p - \left\langle \overline{y}_p \right\rangle\right) + \sum_1^n f_p \bullet \overline{x_{\mathrm{sp}} y_{\mathrm{sp}}} \quad (6)$$

where f_p is the area fraction of the p^{th} patch, n is the number of all patches, $\overline{x}_p$ and $\overline{y}_p$ represent the average value for the p^{th} patch, x_{sp} and y_{sp} represent the sub-patch fluctuations for the p^{th} patch, and $\left\langle \overline{x}_p \right\rangle$ and $\left\langle \overline{y}_p \right\rangle$ represent the grid-level average value.

In this study, we focus on the surface boundary conditions for the mean turbulent heat flux (i.e. latent heat and sensible heat flux) and three (co-)variances that included temperature variance ($\left\langle \theta'^2 \right\rangle$), humidity variance ($\left\langle q'^2 \right\rangle$) and temperature-humidity co-variance ($\langle \theta' q' \rangle$), which are used as the lower boundary conditions for atmospheric turbulence parameterization of E3SM (Xie et al., 2018).

2.5 Experimental design and analysis

A series of offline ELM simulations with different configurations, as summarized in Table 2, were designed and conducted for the four 0.5° grids of the study area to investigate the effects of sub-grid topography on surface energy balance and boundary conditions. Three different sub-grid topographic representations (D, T and 1KM) and two different schemes of sub-grid topographic effects on solar radiation (TOP and PP) were considered in the simulations. The 1 km land surface parameters generated in Section 2.2 were used to derive the 1 km ELM surface dataset. Each ELM grid cell in the 1KM configuration has a single PFT and its own unique soil characteristics. The surface dataset for the D and T configurations was generated using column fraction- and PFT fraction-weighted average methods respectively for soil and vegetation variables to upscale the 1 km surface dataset. For the T configuration, column and PFT fractions for each topounit were calculated and thus vegetation and soil characteristics of each topounit are different. For the 1KM configuration, the topographic factors needed for the TOP scheme were

derived from the 1 km topographic factor dataset introduced in Sections 2.2 and 2.3. For the D configuration, 1 km topographic factors were averaged to grid (0.5°)-level, while for the T configuration, 1 km topographic factors were averaged to topounit-level.

All simulations used the prescribed satellite phenology (SP) mode and the 0.5° × 0.5° Global Soil Wetness Project dataset (GSWP3) (Dirmeyer et al., 2006) was used as the meteorological forcing data. The spatial heterogeneity of the atmospheric forcing data was not considered in the study by using the same atmospheric forcing datasets for all 1 km grids (in the 1KM configuration) and different topounits (in the T configuration). Model outputs were saved at half-hourly time step. Simulations for all model configurations were performed for 31-years from 1980-2010. The first 20 years were considered as model spin up and the simulation outputs from 2000-2010 were used in the subsequent analysis.

To further disentangle the contributions of vegetation and soil, additional topounit-based simulations with/without topounit-dependent vegetation and with/without soil variations were conducted (Table 3). Considering that the differences between TOP and PP in the simulated surface energy balance terms are small for the T configurations (see Section 3.2), only the TOP solar radiation parameterization was used in the sensitivity experiments. Specifically, these topounit-based experiments consisted of heterogeneous vegetation and soil (V+S), only heterogeneous soil (S), only heterogeneous vegetation (V), and no heterogeneity in vegetation and soil (N). Other settings were the same as the simulations in Table 2.

2. **Table 2. Model configurations with different sub-grid topographic representations for each 0.5° × 0.5° grid.**

@ >p(- 14) * >p(- 14) * >p(- 14) * >p(- 14) * >p(- 14) * >p(- 14) * >p(- 14) * >p(- 14) * @

56. Case ID

&

57. Representations of sub-grid topography

&

58. Solar radiation parameterization

&

59. No. of grid cells

&

60. No. of elevation bands

&

61. Spatial resolution

& &

3.

&

4.

&

5.

&

6.

&

7.

&

8. Vegetation

&

9. Soil

&

10. Atmospheric forcing

11. D_PP

&

12. Default

&

13. PP

&

14. 1

&

15. 1

&

16. Sub-grid

&

17. 0.5°

&

18. 0.5°

D_TOP &

19. Default

&

20. TOP

&

21. 1

&

22. 1

&

23. Sub-grid

&

24. 0.5°

&

25. 0.5°

26. T_PP

&

27. Topounit

&

28. PP

&

29. 1

&

30. 11

&

31. Sub-topounit

&

32. Topounit

&

33. 0.5°

34. T_TOP

&

35. Topounit

&

36. TOP

&

37. 1

&

38. 11

&

39. Sub-topounit

&

40. Topounit

&

41. 0.5°

42. 1KM_PP

&

43. 1 km

&

44. PP

&

45. 50×50

&

46. 1

&

47. 1 km

&

48. 1 km

&

49. 0.5°

50. 1KM_TOP

&

51. 1 km

& TOP & 50×50 &

52. 1

&

53. 1 km

&

54. 1 km

&

55. 0.5°

62. **Table 3. Sensitivity experiments under the T configurations and TOP solar radiation scheme with/without considerations of vegetation or soil heterogeneity for each 0.5° × 0.5° grid.**

@ >p(- 14) * >p(- 14) * >p(- 14) * >p(- 14) * >p(- 14) * >p(- 14) * >p(- 14) * >p(- 14) * @

97. Case ID

&

98. Representations of sub-grid topography

&

99. Solar radiation parameterization

&

100. No. of grid cells

&

101. No. of elevation bands

&

102. Spatial resolution

& &

63.

&

64.

&

65.

&

66.

&

67.

&

68. Vegetation

&

69. Soil

&

70. Atmospheric forcing

71. V+S

&

72. Topounit

&

73. TOP

&

74. 1

&

75. 11

&

76. Sub-topounit

&

77. Topounit

&

78. 0.5°

79. S

&

80. Topounit

& TOP & 1 &

81. 11

&

82. Sub-grid

&

83. Topounit

&

84. 0.5°

85. T

&

86. Topounit

& TOP & 1 &

87. 11

&

88. Sub-topounit

&

89. 0.5°

&

90. 0.5°

91. N

&

92. Topounit

& TOP & 1 &

93. 11

&

94. Sub-grid

&

95. 0.5°

&

96. 0.5°

The surface energy balance terms were directly outputted from the aforementioned simulations and the surface boundary conditions for scalar (co-)variances were calculated at a half-hourly scale using the methods described in Section 2.4. Specifically, net solar radiation (R^s_{net}), snow cover fraction (f_{snow}), surface temperature ($\mathrm{T_s}$), latent heat flux ($\mathrm{F_{lh}}$), sensible heat flux ($\mathrm{F_{sh}}$) and gross primary productivity (GPP) were used in the analysis. Based on the Stefan-Boltzmann law and the assumed surface emissivity of 1.0, the emitted longwave radiation was used to derive $\mathrm{T_s}$. The 11-year averaged daily values from 2000-2010 were calculated. Then their mean value (*mean*), standard deviation (*std*) and coefficient of variation (*cv*) were used to describe the effects of sub-grid heterogeneity on the surface energy balance terms and turbulent heat flux. For the simulations with different configurations, *mean* and *std* were derived by

$$mean = \frac{\sum_1^N w_i \bullet x_i}{\sum_1^N w_i} \quad (7)$$

$$std = \sqrt{\frac{\sum_1^N w_i(x_i - mean)^2}{\sum_1^N w_i}} \quad (8)$$

where N is the number of sub-grid cells, x represents the variables of interest (e.g., latent heat and sensible heat flux), x_i is the value of the i-th sub-grid cell and w_i is the area fraction of type i. For the 1KM configuration, $w_i = 1.0$. The cv is calculated as

$$cv = \frac{\text{std}}{\text{mean}} \quad (9)$$

In addition, 1KM_TOP was used as a reference in the analysis and the correlation coefficient (R), normalized bias (nBias) and normalized root mean square deviation (nRMSD) were used to evaluate the agreements between the different configurations with the reference simulation. Specifically, nBias and nRMSD are calculated as

$$nBias = \frac{\sum_1^N (x_{\text{other}} - x_{1km\_TOP})}{N \bullet IQR} \quad (10)$$

$$nRMSE = \frac{\sqrt{\sum_1^N (x_{\text{other}} - x_{1km\_TOP})^2 / N}}{\text{IQR}} \quad (11)$$

where N is the available number of target variable x, x_{1km_TOP} and x_{other} are the target variable values for 1KM_TOP and other cases, respectively, and IQR is the difference between the 75th and the 25th percentiles of x_{1km_TOP}.

3 Results

3.1 High-resolution simulations

TOP and PP have large differences in R^s_{net} for the 1KM configuration. The spatial pattern of R^s_{net} in the winter for the four grids using PP (top row of Figure 3) is related to their PFT distributions (Figure 1c). TOP has more fragmented spatial distributions than PP for all the four grids (middle row of Figure 3), and TOP may absorb larger or smaller solar radiation than PP depending on the local topography (bottom row of Figure 3). The difference between TOP and PP is less pronounced for G3 as compared to the other grids, which is related to their respective topographic characteristics (Figure 1a-b). The difference in R^s_{net} for G1 and G4 can reach up to 40 W/m^2. The seasonal variations and spatial patterns in TOP and PP are similar for G1(top and middle rows of Figure 4). The southwestern regions have larger R^s_{net}, while the northeastern regions have smaller R^s_{net}, which follow the spatial distribution of the PFTs (Figure 1c). This spatial difference is because grass in the northeastern regions has higher land surface albedo than forest in the southwestern regions. The smaller R^s_{net} of the eastern regions in winter is caused by the larger f_{snow} (Figure 5a). The difference between TOP and PP shown in the bottom row of Figure 4 is larger in winter and autumn than summer. The subsequent analysis mainly fucuses on G1 for winter.

There are also large differences between TOP and PP in f_{snow}, T_s, turbulent heat flux and GPP (Figure 5). The spatial patterns of all these

variables for both TOP and PP in the top and middle rows of Figure 5 generally follow the spatial variabilities of PFTs (Figure 1c), but TOP is more fragmented than PP, as affected by local topography. The difference between TOP and PP in f_{snow} shows an opposite trend with R^s_{net} (bottom row of Figure 3), which can be larger than 0.2 (bottom row of Figure 5a). In contrast, the difference in T_s presents a similar spatial pattern with R^s_{net}, and can be as large as 2 K (bottom row of Figure 5b). This further leads to the differences in turbulent heat flux between TOP and PP with larger differences in F_{sh} than F_{lh} (bottom row of Figures 5c-d). The differences in F_{sh} and F_{lh} can be large as 10 and 20 W/m^2, respectively. GPP is also affected by the sub-grid topographic effects, although the difference between TOP and PP is not significant and is within 0.5 umol m^{-2} s^{-1} (bottom row of Figure 5e).

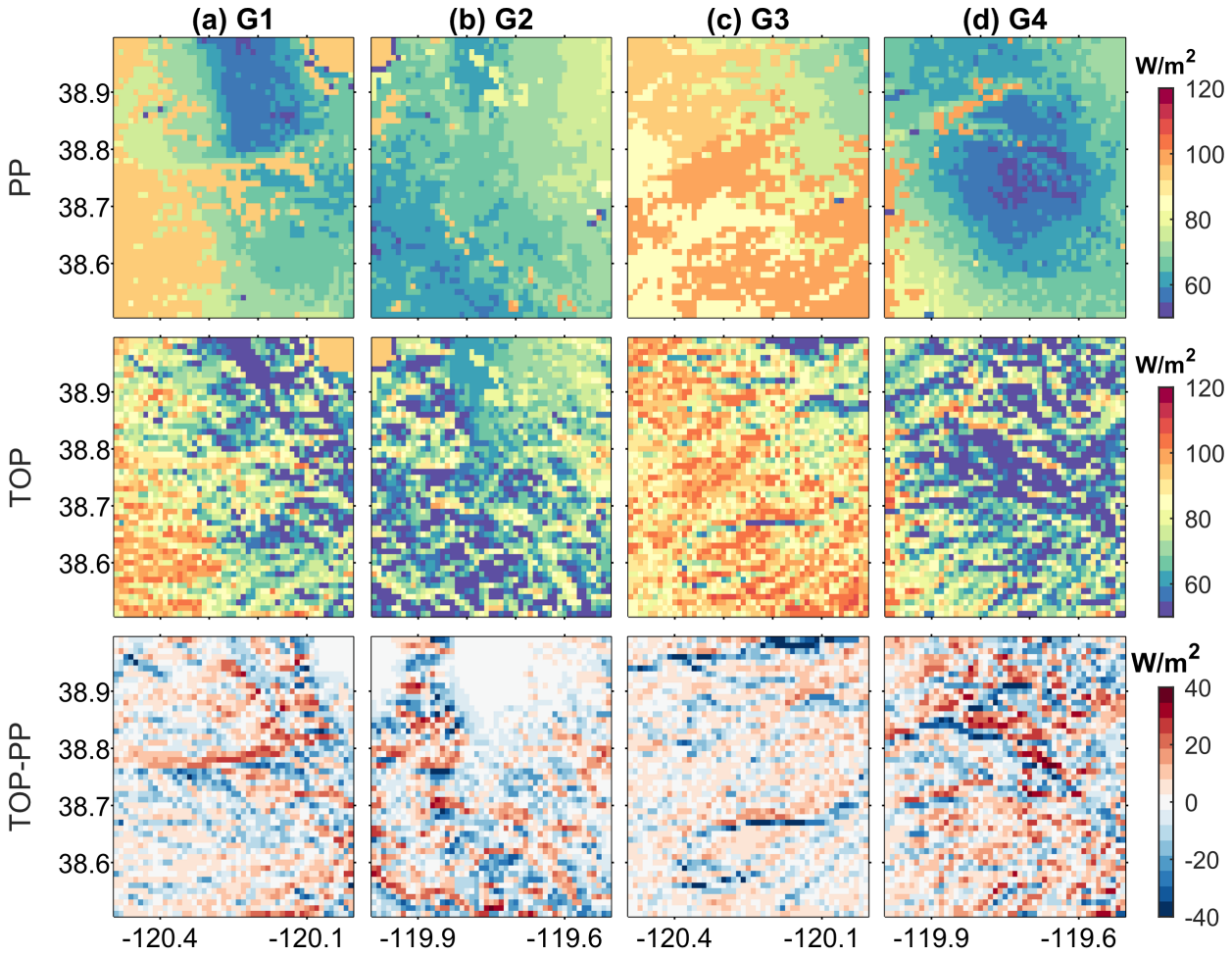

Figure 3. Simulated net solar radiation (R^s_{net}) for PP (top row), TOP (middle row), and their differences (bottom row) during winter (DJF) for different grids: (a) G1, (b) G1, (c) G3, and (d) G4.

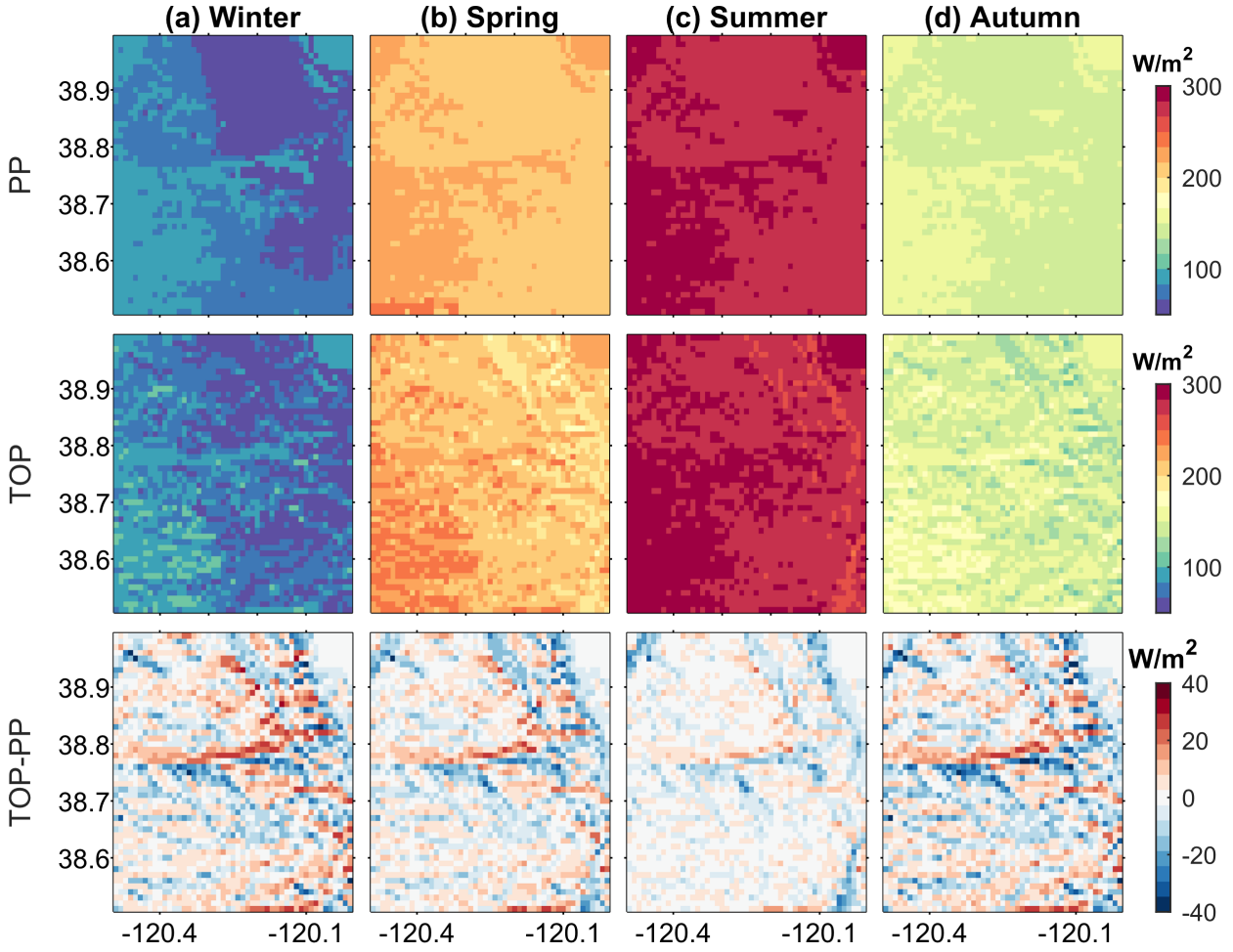

Figure 4. Simulated net solar radiation (R^s_{net}) for PP (top row), TOP (middle row) and their differences (bottom row) for G1 in different seasons: (a) winter (DJF), (b) spring (MAM), (c) summer (JJA), and (d) autumn (SON).

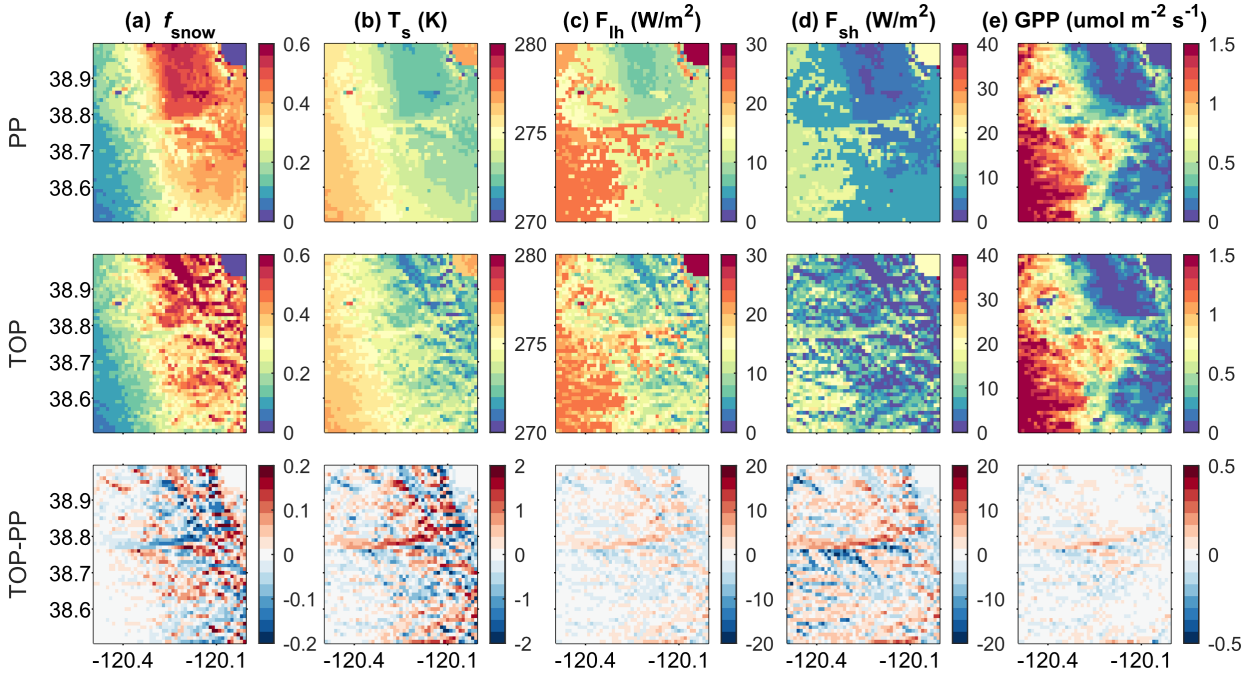

Figure 5. PP (top row) and TOP (middle row) simulation and their differences (bottom row) for (a) snow cover fraction (f_{snow}), (b) surface temperature (T_s), (c) latent heat (F_{lh}), (d) sensible heat (F_{sh}) flux, and (e) gross primary productivity (GPP) in winter (DJF) for G1.

3.2 Effects on surface energy balance

Solar radiation parameterizations (i.e., TOP and PP) have relatively small impacts on surface energy balance in the coarse grid-scale (0.5°). The differences in *mean* and *std* between TOP and PP for the D and T configurations (represented by blue and orange color bars in Figure 6) are small, and thus the results for D_PP and T_PP are excluded from the subsequent analysis. For the 1KM simulation, the *mean* differences between TOP and PP are relatively small (Figure 6), but the *std* differences cannot be neglected. For instance, the *std* differences in R^s_{net} and T_s can reach up to 7.8 W/m^2 and 0.45 K, respectively (Figure 6b,f).

The representations of sub-grid topography have some impacts on the *mean* values of surface energy balance terms and turbulent heat flux for all four grids (i.e., G1-G4). Taking G1 as an example (Figure 7), for R^s_{net}, D_TOP can have differences larger than 14 W/m^2 compared to 1KM_TOP, and T_TOP is closer to 1KM_TOP in winter, while their differences are small in other seasons. Compared to 1KM_TOP, for f_{snow}, the biases of both D_TOP

and T_TOP can be larger than 0.1 in winter. For T_s, their negative biases can reach up to 0.8 K for all seasons. For F_{lh} and F_{sh}, the biases can be as large as 6-8 W/m^2 for all seasons, and for GPP, D_TOP can have a large bias of above 0.7 umol m^{-2} s^{-1} in summer, while the bias of T_TOP is smaller than 0.4 umol m^{-2} s^{-1}. For all the variables, 1KM_PP shows small differences from 1KM_TOP for all seasons. Similar results are obtained from G2-G4 (Figures S1-S3). These grid-scale differences are generally smaller than the differences between TOP and PP at the 1 km scales (Figures 3-5).

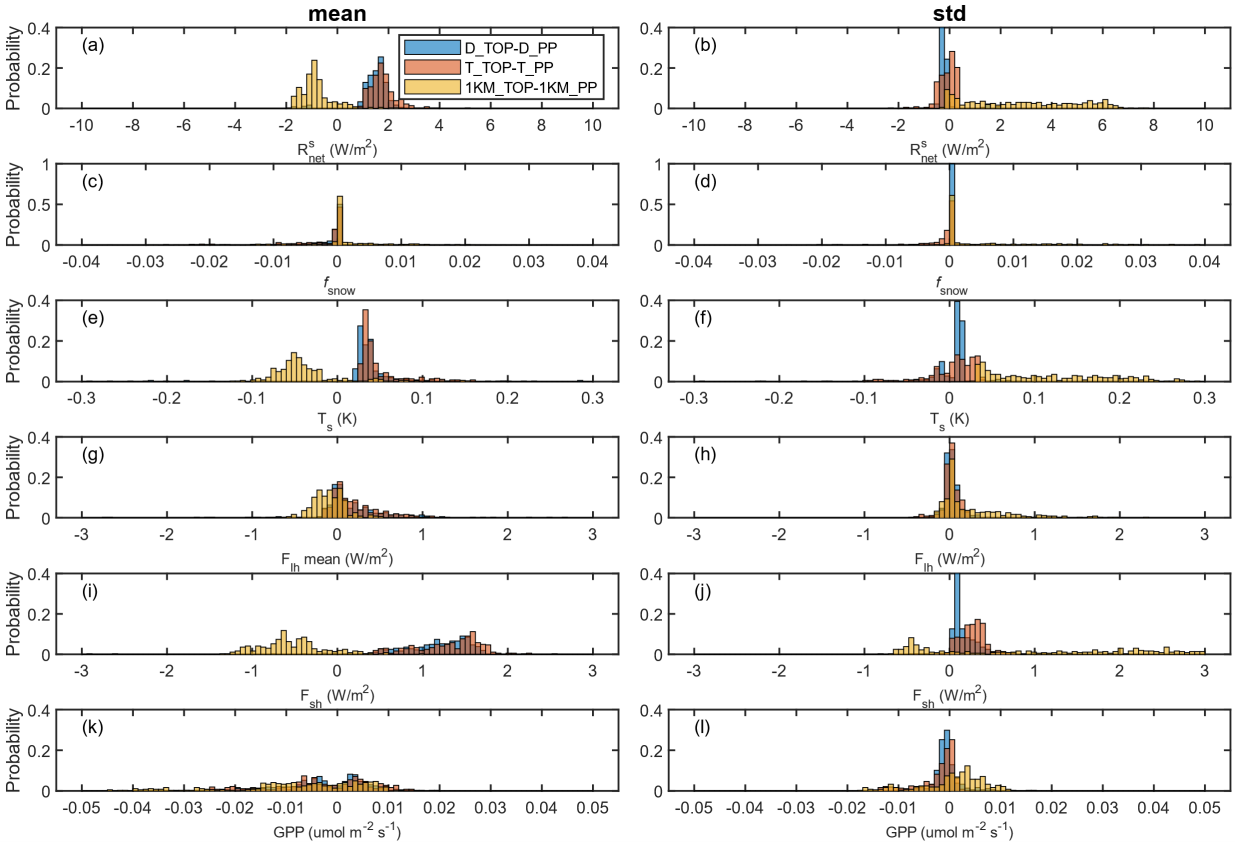

Figure 6. Statistical histograms of the *mean* and *std* differences between TOP and PP in R^s_{net}, f_{snow}, T_s, F_{lh}, F_{sh} and GPP over G1 under different representations of sub-grid topography: D (blue), T (orange) and 1KM (yellow). The bar color is semi-transparent to show the overlapping regions.

The *std*, and *cv* values of surface energy balance and turbulent heat flux within one grid show large differences under different representations of sub-grid topography (Figures 8 and S4-S7). For *std* over G1, the magnitudes of nearly all variables under different cases have large differences. For R^s_{net}, f_{snow}, T_s and GPP, 1KM_TOP has larger *std* values than

other cases, while for F_{lh} and F_{sh}, 1KM_TOP has smaller *std* values than D_TOP and T_TOP. Overall T_TOP shows better agreements with the reference 1KM_TOP than D_TOP. For instance, the maximum f_{snow} biases of D_TOP and T_TOP are 0.22 and 0.11, respectively, and the GPP bias of D_TOP can be larger than 1 umol m^{-2} s^{-1} in spring and summer, while the bias of T_TOP is within 0.3 umol m^{-2} s^{-1}. Different from the *mean*, the *std* for 1KM_PP has some differences with 1KM_TOP especially for R^s_{net}. Specifically in winter and spring, the maximum *mean* and *std* differences in R^s_{net} between 1KM_PP and 1KM_TOP are 2.6 and 7.8 W/m^2, respectively. Similar results for G2-G4 are obtained (Figures S4-S6). For *cv*, the differences between different cases in nearly all variables are more significant in winter than in summer (Figure S7), and similarly, T_TOP is more consistent with 1KM_TOP than with D_TOP.

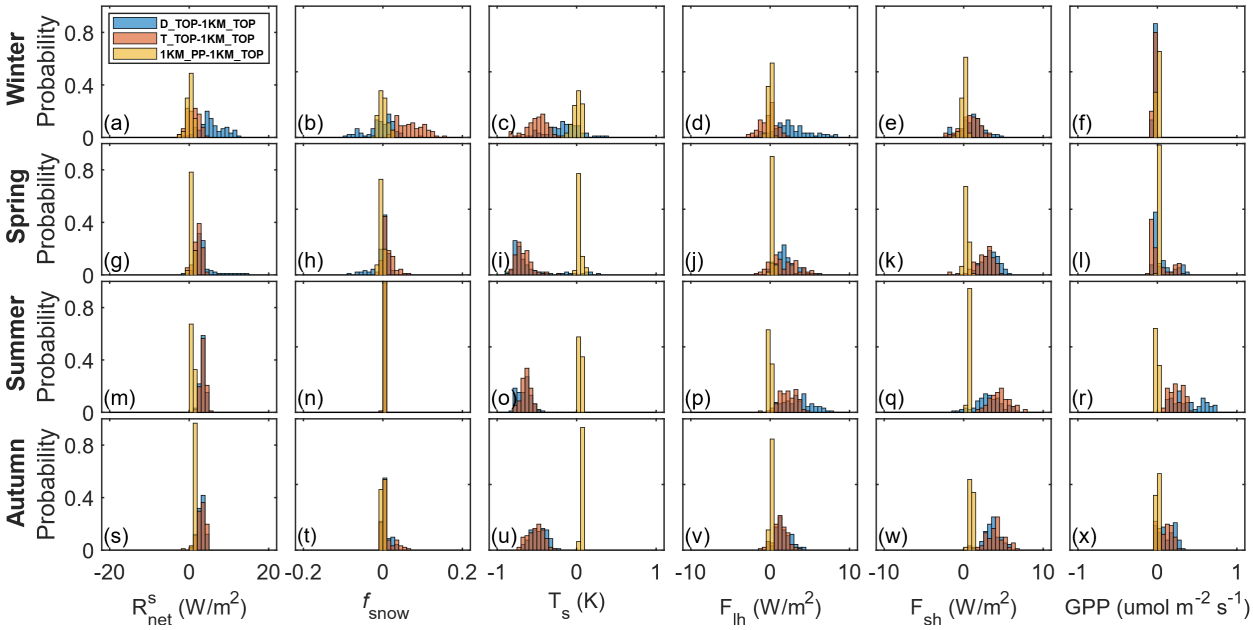

Figure 7. Statistical histograms of the *mean* differences in R^s_{net}, f_{snow}, T_s, F_{lh}, F_{sh} and GPP between different cases of G1 for different seasons. Here, the differences were calculated as the differences between other cases and 1KM_TOP. The bar color is semi-transparent to show the overlapping regions.

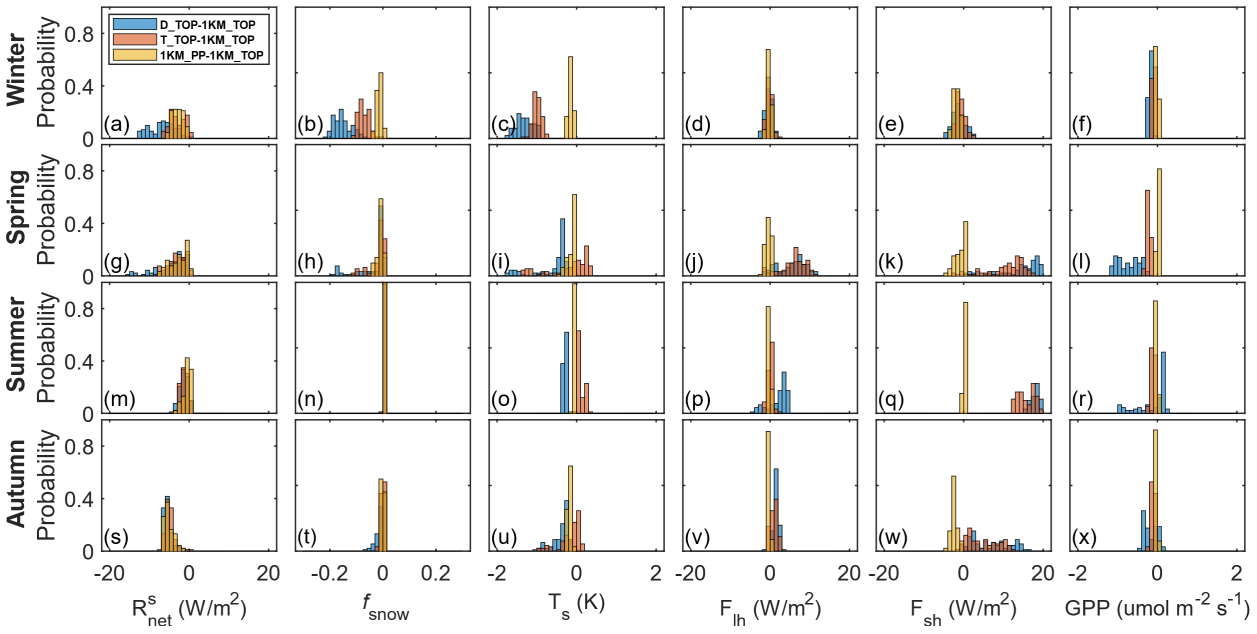

Figure 8. Same as Figure 6, except for standard deviation (*std*).

3.3 Effects on surface boundary conditions for scalar (co-)variances

The sub-grid topographic representations in ELM have large impacts on the surface boundary conditions of scalar (co-)variances especially in winter (Figures 9 and 10). For the HET methods in winter, both D_TOP and T_TOP have lower agreement with 1KM_TOP than 1_km_PP. D_TOP has the lowest R values and the highest nBias and nRMSD values for all scalar (co)-variances. For instance, for $\langle \theta'^2 \rangle$, the nBias value of D_TOP is -146%, while that of T_TOP is -115%. 1KM_PP is more consistent with 1KM_TOP and the R values are higher than 0.95 and the nBias values are ~10% for all the three (co-)variances. The sub-grid topographic effects on local solar radiation in winter leads to some differences in scalar (co-)variances between 1KM_PP and 1KM_TOP (Figure 9c,f,i). Similar results are obtained for G2-G4 in winter (Figures S8-S10). For the HET methods in summer (Figure 10), T_TOP also shows slightly better agreements with 1KM_TOP than D_TOP in all three statistical metrics. The 1KM_PP has high correlations and low bias for all three scalar (co)-variances. While the nRMSD values for 1KM_PP are low for $\langle \theta'^2 \rangle$ and $\langle \theta' q' \rangle$, they are large for $\langle q'^2 \rangle$. For the HOM methods, T_TOP performs better than D_TOP in winter (Figure S11) and all cases show high correlations with 1KM_TOP in summer (Figure S12). Further comparisons of the seasonally-averaged diurnal cycles of scalar (co-)variances under different cases show that T_TOP is closer to the reference case than D_TOP for both

the HET and HOM methods in both summer and winter (Figures 11 and S13). In winter, the biases of D_TOP and T_TOP in the three (co-)variances are smaller than zero and follow similar diurnal cycles. The biases of $\left\langle \theta'^2 \right\rangle$ are the smallest at noon and the largest at night, while those of $\left\langle q'^2 \right\rangle$ and $\langle \theta' q' \rangle$ are the largest at noon and the smallest at night. In summer, the biases in $\left\langle q'^2 \right\rangle$ and $\langle \theta' q' \rangle$ are larger in the morning and evening (Figure 11d,f), possibly caused by the large variability of humidity during these periods.

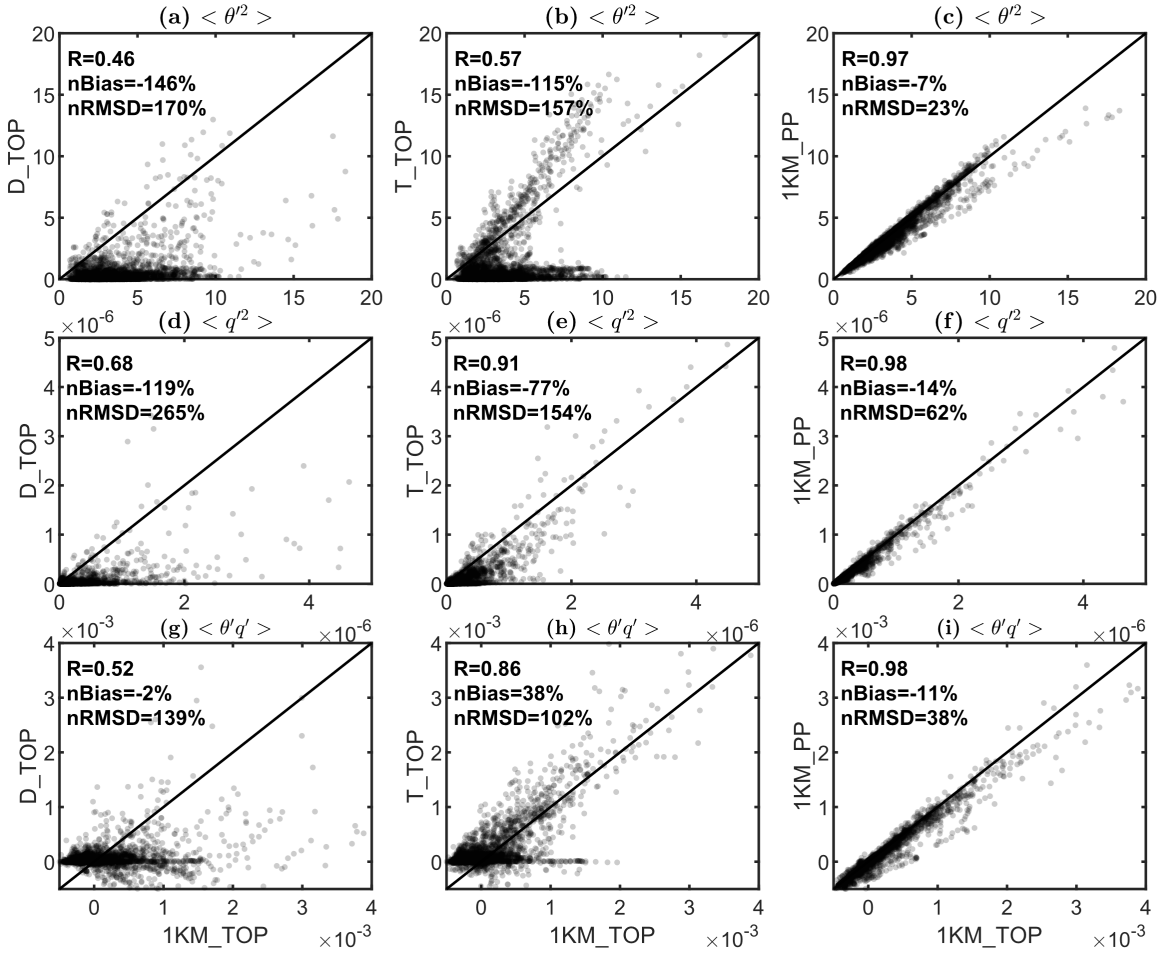

Figure 9. Comparisons of 1KM_TOP simulated (a-c) temperature variance ($\left\langle \theta'^2 \right\rangle$), (d-e) humidity variance ($\left\langle q'^2 \right\rangle$), and (g-i) temperature-humidity covariance ($\langle \theta' q' \rangle$) in winter (DJF) over G1 against simulated values from D_TOP, T_TOP and 1KM_PP model configurations. The (co-)variances were derived using the HET methods introduced in Section 2.4; and R, nBias and nRMSD

were shown in each sub-plot.

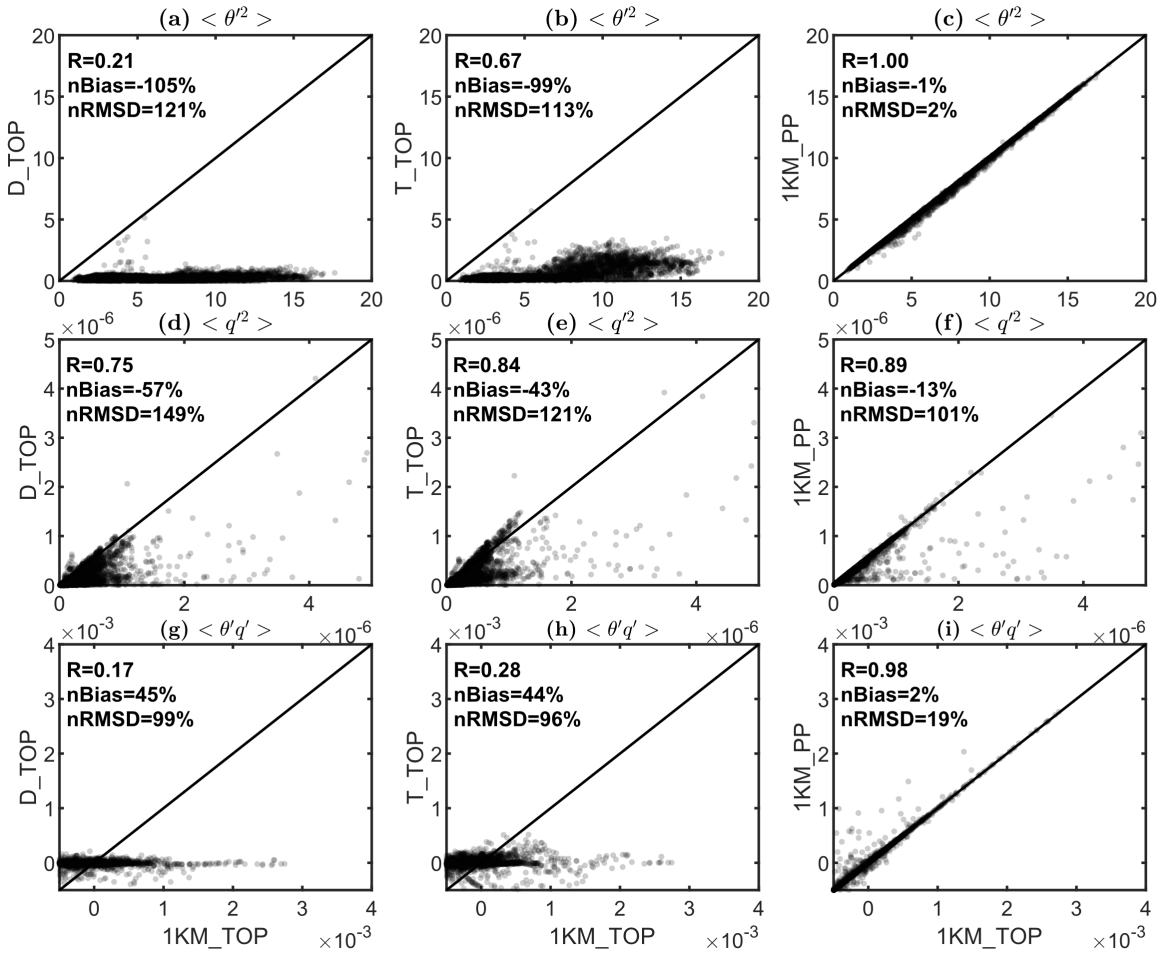

Figure 10. Same as Figure 8, except for summer (JJA).

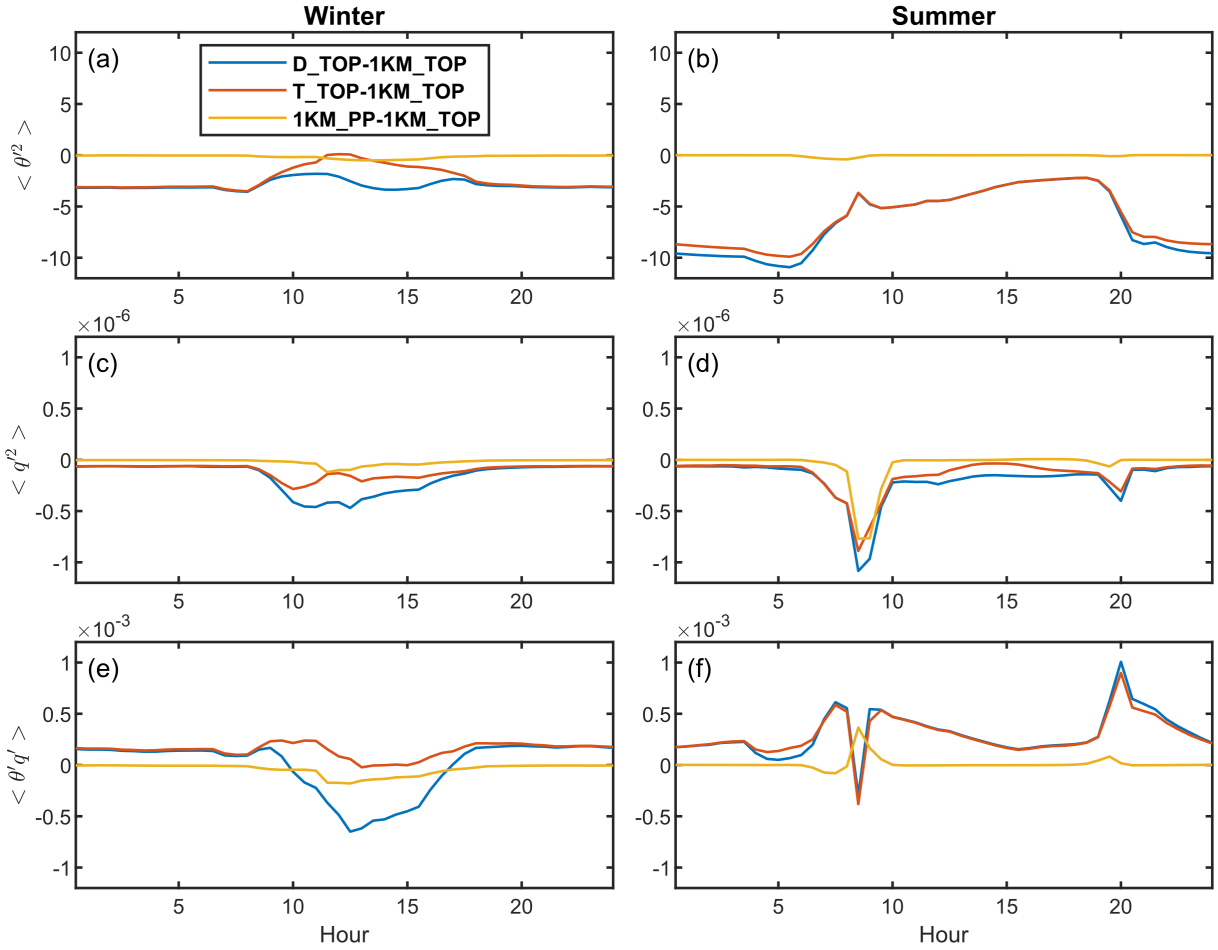

Figure 11. Seasonally-averaged diurnal cycles of the difference in simulated (a & b) temperature variance ($\langle \theta'^2 \rangle$), (c & d) humidity variance ($\langle q'^2 \rangle$), and (e & f) temperature-humidity covariance ($\langle \theta' q' \rangle$) for G1 under different model configurations in winter (DJF) and summer (JJA). Here the local solar time is used and the scalar (co-)variances were derived using the HET methods introduced in Section 2.4. The differences were calculated as the differences between other cases and 1KM_TOP.

3.4 Roles of vegetation and soil heterogeneities

The topounit-scale sensitivity experiments show that vegetation heterogeneity accounts for most of the variations for nearly all the variables (Figures 12 and 13). Generally for R^s_{net}, f_{snow} and T_s, the *mean* and *std* values of the V case are closer to the V+S case than to the S case, while

those of the S case are closer to the N case. These demonstrate that vegetation heterogeneities contribute more to the variability of $R^s_{\rm net}$, $f_{\rm snow}$ and $\rm T_s$, than soil heterogeneity. For $\rm F_{lh}$, $\rm F_{sh}$ and GPP, both soil and vegetation heterogeneities contribute to the differences in *mean* values (Figure 12), but vegetation heterogeneity mainly accounts for the differences in *std* values (Figure 13). These demonstrate that topography-relevant PFT distributions, LAI and SAI characteristics contribute a lot to the *mean* and *std* values of the surface energy balance terms.

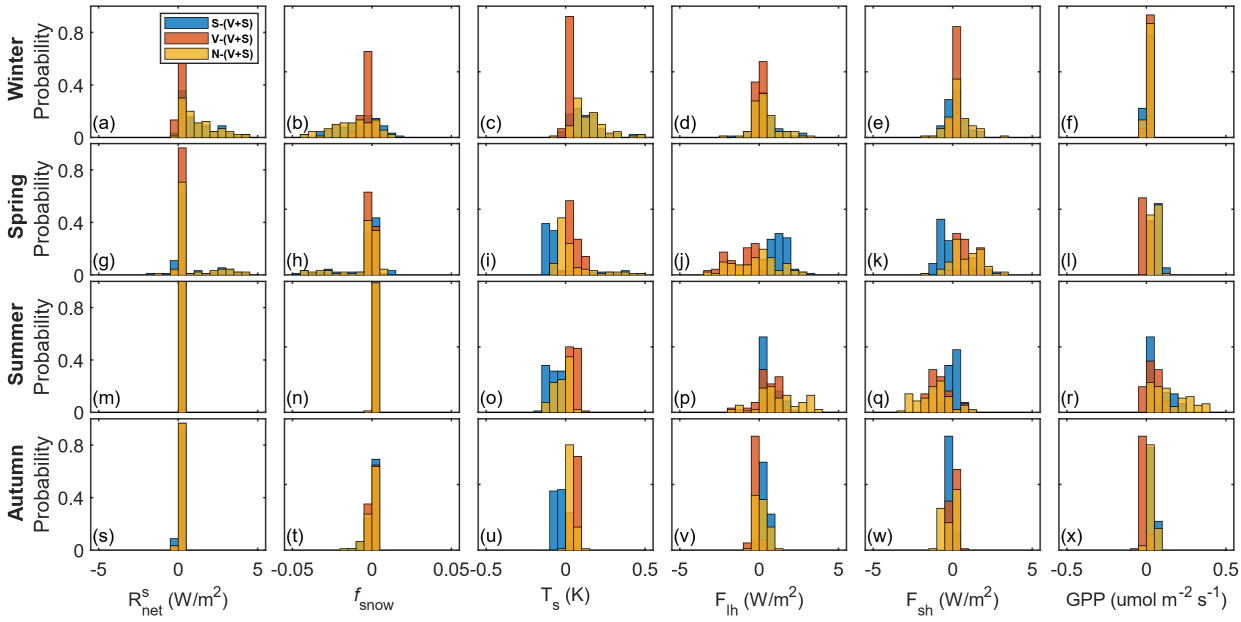

Figure 12. The differences between different cases (V+S, S, V and N) in the *mean* values of $R^s_{\rm net}$, $f_{\rm snow}$, $\rm T_s$, $\rm F_{lh}$, $\rm F_{sh}$ and GPP within one grid for G1. Here, the V+S case is used as a reference and thus the differences were calculated as the differences between other cases and V+S case. The bar color is semi-transparent to show the overlapping regions.

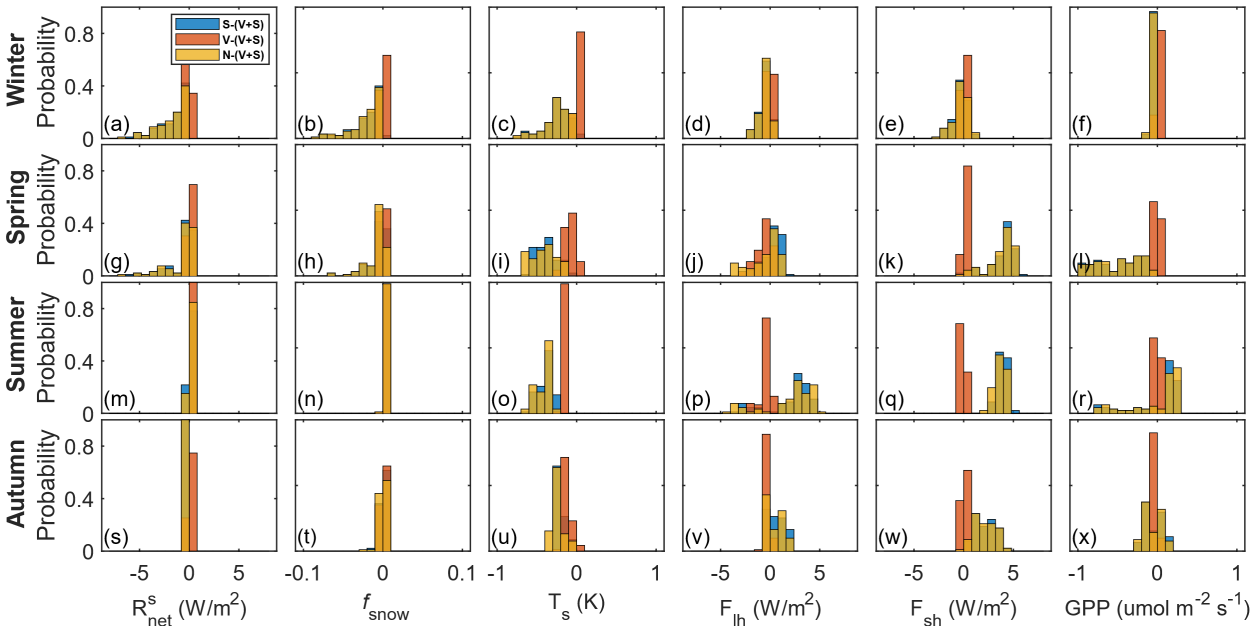

Figure 13. Same as Figure 12, except for *std*.

4 Discussion

Sub-grid topography has large impacts on the spatial distributions of surface energy balance. The spatial patterns of the differences between TOP and PP generally follow the topographic distributions (Figures 3-5). The sub-grid topographic effects on radiation are significant at 1 km spatial resolution. When aggregated to a coarse scale (e.g., 0.5° in this study), the differences between TOP and PP become small because the differences for sunny and shaded slopes offset each other (Zhao et al., 2016), but they still cannot be neglected especially in winter (Figure 7). The differences between TOP and PP are also dependent on the seasons (Figure 4), and are more pronounced in winter due to the snow cover and the strong shadowing effects caused by large solar zenith angles (Hao et al., 2021). These results are similar to previous studies over Sierra Nevada that used WRF (Gu et al., 2012; Liou et al., 2013) and CLM4 (Lee et al., 2015). These differences in surface energy balance can further affect atmospheric processes such as cloud formation and precipitation (Lee et al., 2015; Liou et al., 2013) that needs further investigations by performing E3SM simulations with active atmosphere and land components. GPP is also affected by the sub-grid topography (Figure 5), which underscores the necessity of accounting for sub-grid topographic heterogeneity when simulating GPP over complex terrain (Xie et al., 2021). However, the lateral surface and sub-surface flows from uplands to lowlands were neglected in the simulations reported here, which can also impact the simulation of energy and water fluxes in LSMs (Fan et al., 2019; Ji et al., 2017).

Different representations of sub-grid topography in LSMs affect the surface energy balance and surface boundary conditions. The *mean* values of surface energy balance terms and turbulent heat flux are affected by the representations of sub-grid topography (Figure 7). The *std* values also show large dependences on the representations of sub-grid topography (Figure 8) and these results are consistent with those reported in (Liu et al., 2017). The high-order scalar (co-)variances for the HOM methods are identical for the different representations of sub-grid topography (Figures S11-S13), while there are large differences between different representations of sub-grid topography for the HET methods (Figures 9-11). The large differences in the HET methods are expected to result in large differences in surface boundary conditions, which could further affect the PBL, atmospheric, and cloud dynamics (Chen et al., 2020). T configuration shows better agreements with the 1KM simulations than the D configuration because topounit can better describe the topography-dependent vegetation and soil distributions. In our study area, the differences between the D and T configurations are mainly contributed by topography-dependent vegetation distribution (Figures 12 and 13). However, how the topography-dependent vegetation and soil heterogeneities affect the surface energy balance in other regions needs further investigation. These underline the feasibility and importance of implementing the sub-grid topographic structure in LSMs.

Further optimizing the representations of sub-grid topography is possible as more high-resolution datasets of land surface parameters are available. In the current scheme of topounit in ELM, the topounit number for one grid is spatially variable, the maximum possible number of topounits is set as 12, and the actual number of topounit is determined only by the topographic complexity within a grid (Tesfa and Leung, 2017). For instance, the four grids over the study area include 11 topounits (Figure 2). A spatially variable number of topounits within a grid will reduce the computational burden while attempting to accurately capture the sub-grid heterogeneity of topography. The sensitivity of the topounit's ability of mimicking the realistic conditions to the number of topounits needs to be further analyzed. There exist other approaches to generate topounits to parsimoniously capture sub-grid heterogeneity in topography that account for multiple sources of sub-grid heterogeneities. A topographic sub-grid tool for mountain (TopoSUB) was proposed based on a multi-dimensional informed sampling procedure, where the elevation, slope, aspect and sky view factor were used to represent the topographic characteristics (Fiddes and Gruber, 2012). Similarly, a sub-grid classification method (SGC) was also developed to account for both topographic and vegetation variabilities, but it only considered the differences in elevation (Ke et al., 2013). In addition, a hydrological response unit (HRU)-based structure was developed based on the K-means clustering algorithm (Chaney et al., 2016). Different HRUs have different characteristics of LULC, soil, topography and meteorology forcing. For improving our understanding of the Earth system over heterogeneous terrain, the sub-grid schemes in LSMs need to fully harness emerging big data from field measurements and remote sensing (Chaney et al., 2018).

There are still some limitations in the study. First, the 0.5° GSWP3 forcing data used in the offline ELM simulations is too coarse to capture the sub-grid heterogeneity due to topography in atmospheric forcings (Tesfa et al., 2020). Meteorological forcing data could account for a large proportion of turbulent heat flux in some cases (Jason Scot et al., 2021). Some atmospheric forcing downscaling methods for mountainous areas (Fiddes et al., 2021; Fiddes and Gruber, 2014; Tesfa et al., 2020) and high-resolution forcing data (e.g., Daymet) (Thornton et al., 2016) make it possible to further consider the topography-induced sub-grid heterogeneity of atmospheric forcings. Especially, Tesfa et al. (2020) developed topography-based methods for downscaling grid-scale precipitation to sub-grid scales, which is essentially coupled with the topounit-based sub-grid structure in ELM for improving land surface modeling over mountainous areas. Second, only offline ELM simulations were performed in this study and the effects of sub-grid topographic heterogeneity on the vertical structure of PBL and atmospheric dynamics need to be further investigated using the Cloud Layers Unified By Binormals model coupled with the E3SM atmospheric model (Xie et al., 2018). Third, generalization of the conclusion from this model-based analysis over four 0.5° × 0.5° grid cells to other regions with heterogeneous terrain needs to be further evaluated.

5 Conclusions

The heterogeneity of sub-grid topography exerts large influence on many land surface processes and further affects atmospheric dynamics. This study used ELM to investigate the impacts of sub-grid topographic representations on surface energy balance and surface boundary conditions for turbulent heat flux and scalar (co-)variances. A series of simulations with three different sub-grid topographic representations (i.e., D, T and 1KM) and two different treatments of the sub-grid topographic effects on solar radiation (i.e., TOP and PP) were carried out in four representative 0.5° grids. The results show that topography has large impacts on the spatial distribution of surface energy balance terms and TOP and PP have significant differences at 1 km resolution in simulating surface energy balance, f_{snow} and $\mathrm{T_s}$, which depend on seasons and local topography. The differences in the mean values are relatively small when aggregated to 0.5° grid-scales because the positive-negative differences for sunny and shaded slopes offset each other. Different representations of sub-grid topography can also affect the surface energy balance and surface boundary conditions. As compared to the D configuration, the T configuration can more accurately capture the effects of sub-grid topographic heterogeneity on the mean values and standard deviations of surface energy balance terms as well as surface boundary conditions for turbulent heat flux and scalar (co-)variances. The findings in this study underline the importance of improving the representations of the sub-grid topographic heterogeneity in LSMs over complex terrain.

Acknowledgments

This research has been supported by the U.S. Department of Energy, Office of Science, Office of Biological and Environmental Research, Earth System Model

Development program area, as part of the Climate Process Team projects (73743, 73742). This study was also supported by the Atmospheric Administration (NOAA) under award numbers NOAA-OAR-CPO-2019-2005530. The reported research was conducted at the Pacific Northwest National Laboratory, which is operated for the U.S. Department of Energy by Battelle Memorial Institute under contract DE-AC05-76RL01830. This research used the computational resources of the National Energy Research Scientific Computing Center, a DOE Office of Science User Facility supported by the Office of Science of the U.S. Department of Energy.

Availability Statement

The ELM code are available publicly at https://github.com/E3SM-Project/E3SM (last access: 28 September 2021) and the code for TOP solar radiation parameterizations used in this paper is available at http://doi.org/10.5281/zenodo.4549401. Codes and data to reproduce results and plot figures are publicly available at https://github.com/daleihao/subgrid_topographic_representations_in_ELM.git. All MODIS, WorldClim V1, Soilgrid v2 and SRTM DEM data introduced in Table 1 are publicly available at GEE (https://earthengine.google.com/).

References

André, J., De Moor, G., Lacarrere, P. and Du Vachat, R., 1978. Modeling the 24-hour evolution of the mean and turbulent structures of the planetary boundary layer. Journal of Atmospheric Sciences, 35(10): 1861-1883.

Avissar, R. and Chen, F., 1993. Development and analysis of prognostic equations for mesoscale kinetic energy and mesoscale (subgrid scale) fluxes for large-scale atmospheric models. Journal of Atmospheric Sciences, 50(22): 3751-3774.

Bisht, G., Riley, W.J., Hammond, G.E. and Lorenzetti, D.M., 2018. Development and evaluation of a variably saturated flow model in the global E3SM Land Model (ELM) version 1.0. Geosci. Model Dev., 11(10): 4085-4102.

Bonan, G.B., Levis, S., Kergoat, L. and Oleson, K.W., 2002. Landscapes as patches of plant functional types: An integrating concept for climate and ecosystem models. Global Biogeochemical Cycles, 16(2): 5-1-5-23.

Bou-Zeid, E., Anderson, W., Katul, G.G. and Mahrt, L., 2020. The Persistent Challenge of Surface Heterogeneity in Boundary-Layer Meteorology: A Review. Boundary-Layer Meteorology, 177(2): 227-245.

Brunsell, N.A., Mechem, D.B. and Anderson, M.C., 2011. Surface heterogeneity impacts on boundary layer dynamics via energy balance partitioning. Atmos. Chem. Phys., 11(7): 3403-3416.

Chaney, N.W., Metcalfe, P. and Wood, E.F., 2016. HydroBlocks: a field-scale resolving land surface model for application over continental extents. Hydrological Processes, 30(20): 3543-3559.

Chaney, N.W. et al., 2018. Harnessing big data to rethink land heterogeneity in Earth system models. Hydrol. Earth Syst. Sci., 22(6): 3311-3330.

Chen, J., Hagos, S., Xiao, H., Fast, J.D. and Feng, Z., 2020. Characterization of Surface Heterogeneity-Induced Convection Using Cluster Analysis. Journal of Geophysical Research: Atmospheres, 125(20): e2020JD032550.

de Vrese, P., Schulz, J.-P. and Hagemann, S., 2016. On the Representation of Heterogeneity in Land-Surface–Atmosphere Coupling. Boundary-Layer Meteorology, 160(1): 157-183.

Dearborn, K.D. and Danby, R.K., 2017. Aspect and slope influence plant community composition more than elevation across forest–tundra ecotones in subarctic Canada. Journal of Vegetation Science, 28(3): 595-604.

Dirmeyer, P.A. et al., 2006. GSWP-2: Multimodel Analysis and Implications for Our Perception of the Land Surface. Bulletin of the American Meteorological Society, 87(10): 1381-1398.

Dubayah, R., 1992. Estimating net solar radiation using Landsat Thematic Mapper and digital elevation data. Water Resources Research, 28(9): 2469-2484.

Fan, Y. et al., 2019. Hillslope Hydrology in Global Change Research and Earth System Modeling. Water Resources Research, 55(2): 1737-1772.

Fiddes, J., Aalstad, K. and Lehning, M., 2021. TopoCLIM: Rapid topography-based downscaling of regional climate model output in complex terrain v.1.0. Geosci. Model Dev. Discuss., 2021: 1-27.

Fiddes, J. and Gruber, S., 2012. TopoSUB: a tool for efficient large area numerical modelling in complex topography at sub-grid scales. Geosci. Model Dev., 5(5): 1245-1257.

Fiddes, J. and Gruber, S., 2014. TopoSCALE v.1.0: downscaling gridded climate data in complex terrain. Geosci. Model Dev., 7(1): 387-405.

Fisher, R.A. and Koven, C.D., 2020. Perspectives on the Future of Land Surface Models and the Challenges of Representing Complex Terrestrial Systems. Journal of Advances in Modeling Earth Systems, 12(4): e2018MS001453.

Friedl, M.A. et al., 2002. Global land cover mapping from MODIS: algorithms and early results. Remote Sensing of Environment, 83(1): 287-302.

Giorgi, F. and Avissar, R., 1997. Representation of heterogeneity effects in Earth system modeling: Experience from land surface modeling. Reviews of Geophysics, 35(4): 413-437.

Golaz, J.-C. et al., 2019. The DOE E3SM Coupled Model Version 1: Overview and Evaluation at Standard Resolution. Journal of Advances in Modeling Earth Systems, 11(7): 2089-2129.

Gorelick, N. et al., 2017. Google Earth Engine: Planetary-scale geospatial analysis for everyone. Remote Sensing of Environment, 202: 18-27.

Gu, Y., Liou, K.N., Lee, W.L. and Leung, L.R., 2012. Simulating 3-D radiative transfer effects over the Sierra Nevada Mountains using WRF. Atmos. Chem. Phys., 12(20): 9965-9976.

Guo, H. et al., 2015. CLUBB as a unified cloud parameterization: Opportunities and challenges. Geophysical Research Letters, 42(11): 4540-4547.

Hao, D. et al., 2021. A Parameterization of Sub-grid Topographical Effects on Solar Radiation in the E3SM Land Model (Version 1.0): Implementation and Evaluation Over the Tibetan Plateau. Geosci. Model Dev. Discuss., 2021: 1-23.

Hao, D. et al., 2019. Impacts of DEM Geolocation Bias on Downward Surface Shortwave Radiation Estimation Over Clear-Sky Rugged Terrain: A Case Study in Dayekou Basin, China. IEEE Geoscience and Remote Sensing Letters, 16(1): 10-14.

Hengl, T. et al., 2017. SoilGrids250m: Global gridded soil information based on machine learning. PLOS ONE, 12(2): e0169748.

Hijmans, R.J., Cameron, S.E., Parra, J.L., Jones, P.G. and Jarvis, A., 2005. Very high resolution interpolated climate surfaces for global land areas. International Journal of Climatology, 25(15): 1965-1978.

Jason Scot, S., Andrew, D.B., Paul, A.D. and Nathaniel, W.C., 2021. Semi-coupling of a Field-scale Resolving Land-surface Model and WRF-LES to Investigate the Influence of Land-surface Heterogeneity on Cloud Development. Earth and Space Science Open Archive.

Ji, P., Yuan, X. and Liang, X.-Z., 2017. Do Lateral Flows Matter for the Hyperresolution Land Surface Modeling? Journal of Geophysical Research: Atmospheres, 122(22): 12,077-12,092.

Ke, Y. et al., 2012. Development of high resolution land surface parameters for the Community Land Model. Geosci. Model Dev., 5(6): 1341-1362.

Ke, Y., Leung, L.R., Huang, M. and Li, H., 2013. Enhancing the representation of subgrid land surface characteristics in land surface models. Geosci. Model Dev., 6(5): 1609-1622.

Lawrence, D.M. et al., 2019. The Community Land Model Version 5: Description of New Features, Benchmarking, and Impact of Forcing Uncertainty. Journal of Advances in Modeling Earth Systems, 11(12): 4245-4287.

Lee, J.M., Zhang, Y. and Klein, S.A., 2019a. The Effect of Land Surface Heterogeneity and Background Wind on Shallow Cumulus Clouds and the Transition to Deeper Convection. Journal of the Atmospheric Sciences, 76(2): 401-419.

Lee, W.-L. et al., 2019b. Impact of 3-D Radiation-Topography Interactions on Surface Temperature and Energy Budget Over the Tibetan Plateau in Winter.

Journal of Geophysical Research: Atmospheres, 124(3): 1537-1549.

Lee, W.L., Gu, Y., Liou, K.N., Leung, L.R. and Hsu, H.H., 2015. A global model simulation for 3-D radiative transfer impact on surface hydrology over the Sierra Nevada and Rocky Mountains. Atmos. Chem. Phys., 15(10): 5405-5413.

Lee, W.-L., Liou, K.N. and Hall, A., 2011. Parameterization of solar fluxes over mountain surfaces for application to climate models. Journal of Geophysical Research: Atmospheres, 116(D1).

Leung, L.R., Bader, D.C., Taylor, M.A. and McCoy, R.B., 2020. An Introduction to the E3SM Special Collection: Goals, Science Drivers, Development, and Analysis. Journal of Advances in Modeling Earth Systems, 12(11): e2019MS001821.

Levy, P. et al., 2020. Inference of spatial heterogeneity in surface fluxes from eddy covariance data: A case study from a subarctic mire ecosystem. Agricultural and Forest Meteorology, 280: 107783.

Liou, K.N., Gu, Y., Leung, L.R., Lee, W.L. and Fovell, R.G., 2013. A WRF simulation of the impact of 3-D radiative transfer on surface hydrology over the Rocky Mountains and Sierra Nevada. Atmos. Chem. Phys., 13(23): 11709-11721.

Liu, S., Shao, Y., Kunoth, A. and Simmer, C., 2017. Impact of surface-heterogeneity on atmosphere and land-surface interactions. Environmental Modelling & Software, 88: 35-47.

Lyons, T.J. and Halldin, S., 2004. Surface heterogeneity and the spatial variation of fluxes. Agricultural and Forest Meteorology, 121(3): 153-165.

Machulskaya, E. and Mironov, D., 2018. Boundary conditions for scalar (co) variances over heterogeneous surfaces. Boundary-Layer Meteorology, 169(1): 139-150.

Maronga, B. and Raasch, S., 2013. Large-Eddy Simulations of Surface Heterogeneity Effects on the Convective Boundary Layer During the LITFASS-2003 Experiment. Boundary-Layer Meteorology, 146(1): 17-44.

Myneni, R.B. et al., 2002. Global products of vegetation leaf area and fraction absorbed PAR from year one of MODIS data. Remote Sensing of Environment, 83(1): 214-231.

Poggio, L. et al., 2021. SoilGrids 2.0: producing soil information for the globe with quantified spatial uncertainty. SOIL, 7(1): 217-240.

Proy, C., Tanré, D. and Deschamps, P.Y., 1989. Evaluation of topographic effects in remotely sensed data. Remote Sensing of Environment, 30(1): 21-32.

Rabus, B., Eineder, M., Roth, A. and Bamler, R., 2003. The shuttle radar topography mission—a new class of digital elevation models acquired by space-

borne radar. ISPRS Journal of Photogrammetry and Remote Sensing, 57(4): 241-262.

Román-Cascón, C. et al., 2021. Surface representation impacts on turbulent heat fluxes in WRF (v.4.1.3). Geosci. Model Dev. Discuss., 2021: 1-51.

Ropars, P. and Boudreau, S., 2012. Shrub expansion at the forest–tundra ecotone: spatial heterogeneity linked to local topography. Environmental Research Letters, 7(1): 015501.

Schneider, T., Lan, S., Stuart, A. and Teixeira, J., 2017. Earth System Modeling 2.0: A Blueprint for Models That Learn From Observations and Targeted High-Resolution Simulations. Geophysical Research Letters, 44(24): 12,396-12,417.

Sellers, P.J., 1985. Canopy reflectance, photosynthesis and transpiration. International Journal of Remote Sensing, 6(8): 1335-1372.

Still, C.J., Berry, J.A., Collatz, G.J. and DeFries, R.S., 2003. Global distribution of C3 and C4 vegetation: Carbon cycle implications. Global Biogeochemical Cycles, 17(1): 6-1-6-14.

Tesfa, T.K., Leung, L.R. and Ghan, S.J., 2020. Exploring Topography-Based Methods for Downscaling Subgrid Precipitation for Use in Earth System Models. Journal of Geophysical Research: Atmospheres, 125(5): e2019JD031456.

Tesfa, T.K. and Leung, L.Y.R., 2017. Exploring new topography-based subgrid spatial structures for improving land surface modeling. Geosci. Model Dev., 10(2): 873-888.

Thornton, P. et al., 2016. Daymet: daily surface weather data on a 1-km grid for North America, version 3. ORNL DAAC, Oak Ridge, Tennessee, USA, USDA-NASS, 2019. 2017 Census of Agriculture, Summary and State Data, Geographic Area Series, Part 51, AC-17-A-51.

Wu, Y. et al., 2009. Impact of Land Surface Heterogeneity on Mesoscale Atmospheric Dispersion. Boundary-Layer Meteorology, 133(3): 367.

Xie, S. et al., 2018. Understanding Cloud and Convective Characteristics in Version 1 of the E3SM Atmosphere Model. Journal of Advances in Modeling Earth Systems, 10(10): 2618-2644.

Xie, X., Chen, J.M., Gong, P. and Li, A., 2021. Spatial Scaling of Gross Primary Productivity Over Sixteen Mountainous Watersheds Using Vegetation Heterogeneity and Surface Topography. Journal of Geophysical Research: Biogeosciences, 126(5): e2020JG005848.

Yang, X. et al., 2019. The Effects of Phosphorus Cycle Dynamics on Carbon Sources and Sinks in the Amazon Region: A Modeling Study Using ELM v1. Journal of Geophysical Research: Biogeosciences, 124(12): 3686-3698.

Zeng, X., Shaikh, M., Dai, Y., Dickinson, R.E. and Myneni, R., 2002. Coupling of the Common Land Model to the NCAR Community Climate Model. Journal

of Climate, 15(14): 1832-1854.

Zhang, N., Williams, Q.L. and Liu, H., 2010. Effects of land-surface heterogeneity on numerical simulations of mesoscale atmospheric boundary layer processes. Theoretical and Applied Climatology, 102(3): 307-317.

Zhao, B. et al., 2016. Impact of buildings on surface solar radiation over urban Beijing. Atmos. Chem. Phys., 16(9): 5841-5852.

Zheng, Y., Brunsell, N.A., Alfieri, J.G. and Niyogi, D., 2021. Impacts of land cover heterogeneity and land surface parameterizations on turbulent characteristics and mesoscale simulations. Meteorology and Atmospheric Physics, 133(3): 589-610.